JOURNAL OF AIRCRAFT
Vol. 34, No. 3, May–June 1997

Multivariable Active Lifting Surface Control Using Strain Actuation: Analytical and Experimental Results

Kenneth B. Lazarus*
Active Control Experts, Inc., Cambridge, Massachusetts 02142
and
Edward F. Crawley† and Charrissa Y. Lin‡
Massachusetts Institute of Technology, Cambridge, Massachusetts 02139

This paper describes an analytical and experimental investigation into the use of active lifting surfaces with distributed strain actuators for dynamic aeroelastic control. A detailed analytical aeroelastic model is developed for analysis and control law design using the Rayleigh–Ritz assumed mode method, kernel function unsteady aerodynamics, and modern state-space techniques. The models are used to design multivariable dynamic compensators for applications such as gust alleviation, command following, and flutter suppression. The effectiveness of the control laws is assessed analytically and verified experimentally through closed-loop wind-tunnel testing. The experiments demonstrate that distributed strain actuation can be effectively employed for aeroelastic control, with gust alleviation of 8-dB broadband and an increase in flutter speed of 11%.

Introduction

THIS work investigates the use of active lifting surfaces with distributed strain actuators for dynamic aeroelastic control. Active lifting surface control is desirable for enhancing aircraft performance, increasing the flight envelope of aircraft with vibration problems, decreasing loads, and improving ride quality.[1] This paper examines active lifting surface control for applications such as gust alleviation, command following, and flutter suppression. Gust alleviation is needed to eliminate unwanted vibrations that cause performance degradation, poor ride quality, and dynamically amplified loads. Command following in bandwidths from quasisteady up to and through the fundamental vibration frequency is desirable for enhancing aircraft performance specifications such as pull-up and roll rates. Finally, flutter suppression is important for increasing the flight envelope of high-performance aircraft.

Traditionally, control of flexible lifting surfaces has been effected through the use of articulated aerodynamic control surfaces such as ailerons or flaperons. A vast body of literature exists concerning the development and implementation of various feedback control schemes that utilize such articulated actuator systems. Researchers have examined traditional aeroelastic control using typical section models and classical control methods.[2–4] The use of more representative models and modern control techniques has been studied for problems such as flutter suppression[5–12] and gust alleviation.[13,14] Recently, the active flexible wing (AFW) has been used to demonstrate the ability of conventional control surfaces and modern control techniques to suppress flutter while performing various maneuvers in wind-tunnel experiments.[15–17]

In contrast to the previously mentioned work, which employs the usual articulated control surface actuators, this research concentrates on an alternative and fundamentally different method of dynamic aeroelastic control. The technique involves the use of induced strain actuators, which are regulated to apply equivalent forces and moments on the lifting surface, to deform the wing and effect dynamic aeroelastic control. Induced strain actuators, such as piezoceramics and electrostrictives, directly deform the structure through electromechanical coupling terms that appear in the actuator constitutive relations. The effectiveness of strain actuation for static aeroelastic control has been investigated with mixed results.[18,19] However, active structures with integrated strain actuators provide a natural and logical mechanism for effecting multiple-actuator dynamic control and for implementing modern model-based control methodologies such as the linear quadratic Gaussian (LQG),[20] H_∞,[21] and optimal projection[22] techniques. Thus, it may be advantageous to use distributed strain actuation for the dynamic control of lifting surfaces.

Strain actuation is advantageous because it can directly control both the shape of and strain in the lifting surface. Thus, two mechanisms by which aeroelastic control can be effected are available. Both the control of aerodynamic forces created by altering the airfoil shape and direct control of the strain in the lifting surface may be used to improve aircraft performance. Specifically, a strain-actuated active lifting surface can be used for gust and load alleviation (i.e., disturbance rejection), flutter and vibration suppression (i.e., plant regulation), and maneuver enhancement (i.e., command following).

The strain-actuated lifting surface test articles are described in the following section, with greater detail in Lazarus and Crawley.[23] The test articles were recently bench-top tested to demonstrate the effectiveness of strain actuation for controlling flexible plate-like components of intelligent structures. The results are presented in Lazarus and Crawley,[24] which also contains the details of the dynamic structural model used to describe the lifting surface test articles. This paper discusses the aeroelastic model developed for the purpose of designing control laws to achieve aeroelastic control using strain actuation. A detailed aerodynamic model is developed from kernel function unsteady aerodynamics. The aerodynamic model is added to the structural model via a rational function approximation, creating an accurate aeroelastic model from which control laws

Presented as Paper 92-2529 at the 1st International Conference on Adaptive Structures, San Diego, CA, Nov. 9–11, 1992; received Nov. 14, 1994; revision received May 12, 1996; accepted for publication Oct. 28, 1996.

*President, 215 First Street. Member AIAA.
†Professor of Aeronautics and Astronautics, Room 37-351, 77 Massachusetts Avenue. Fellow AIAA.
‡Graduate Research Assistant, Room 37-391, 77 Massachusetts Avenue. Student Member AIAA.

can be developed. The analytic model is used to derive high-authority, large-bandwidth multi-input/multi-output (MIMO) compensators based on a quadratic cost function and LQG optimal control theory. Compensators are also designed using frequency domain LQG–LTR techniques. The control schemes are then assessed analytically to determine their closed-loop effectiveness and verified experimentally in closed-loop wind-tunnel experiments. The wind-tunnel experiments show the ability of strain-actuated lifting surfaces to achieve aeroelastic control objectives such as gusts disturbance attenuation, input command following, and flutter suppression.

Test Configuration

The test articles were designed as thin, low-aspect-ratio lifting surfaces. Figure 1 shows a diagram of the strain-actuated active lifting surface test articles. Each article had a span x of 11.5 in. (29.2 cm) and a chord y of 6.0 in. (15 cm), which resulted in an equivalent full-span aspect ratio of 3.83. The thickness-to-chord ratio of the test articles was 0.51%. Two model lifting surfaces were constructed, analyzed, and tested. A 6061 aluminum benchmark article was designed and tested as was a $[+30_2/0]_s$ bending/twist-coupled AS4/3501-6 graphite/epoxy (G/E) plate that exhibited enhanced torsional control. The bending/twist-coupled G/E lifting surface was tested in a wash-in (bending causes an increased angle of attack) configuration.

The Piezoelectric Products Incorporated G-1195 piezoceramic actuators were intended to not only provide actuation, but also to make up a substantial portion of the structure itself. Each of the active test articles had approximately 70% of each surface covered with the surface-bonded piezoceramic strain actuators. The 10-mil (0.254-mm) strain actuators accounted for 31.3 and 52% of the aluminum lifting surface volume and weight, and 30.1 and 62.3% of the G/E lifting surface volume and weight, respectively.

The aluminum plate was later (after all other experiments were completed) modified to flutter within the wind-tunnel operating range. The test article was modified by attaching a lead mass at the wing tip one semichord behind the trailing edge. The mass weighed 285.5 g or 120.9% of the original aluminum test article weight (236.22 g) and was held in place by an 85.7-g aluminum brace, making the total modified-for-flutter aluminum test article mass equal to 157.1% of the nominal aluminum lifting surface. The added weight lowered the fundamental vibration frequency of the modified-for-flutter test article by 57.6% and lowered the flutter speed by 32.3%.

The wind-tunnel experiments were conducted in the Massachusetts Institute of Technology's Department of Aeronautics and Astronautics 1 × 1 ft laminar flow wind tunnel. A wind-tunnel test section, shown in Fig. 2, was constructed to house the lifting surfaces, laser displacement sensors, pitot tube, and gust generator disturbance source. The test section had a width of 8.0 in. (20.3 cm) and a height of 12.0 in. (30.5 cm), and the lifting surfaces were mounted vertically in the middle of the section.

Three Keyence LB-70 laser sensors measured the tip displacement at the leading edge (LE) y_1, midchord (MC) y_2, and trailing edge (TE) y_3 and were located 4.0 in. (10.2 cm) from the test articles. This 4.0-in. standoff distance gave a usable out-of-plane measurement range of plus or minus 1.5 in. (3.81 cm) from the laser sensors, which had a maximum range of 5.5 in. (14.0 cm). It is acknowledged that actual lifting surfaces are not able to take advantage of such displacement measurements. However, actual lifting surfaces do have ample space (not available on the small-scale model lifting surfaces) for accelerometers, the output of which can be integrated to yield measurements equivalent to the displacement measurements made in this study.

The disturbance for the wind-tunnel experiments was supplied by a gust generator, designed and constructed to provide about a 1-deg broadband angle-of-attack variation in the free-stream flow. The gust generator, depicted in Fig. 2, was constructed of three gust vanes made from 0.0625-in.-thick aluminum and a 0.75-in. aluminum push rod. The gust vanes, which had a chord of 4.0 in. and a span of 11.5 in., were placed in the wind-tunnel test section 6.0 in. ahead (measure from the midchord of the lifting surfaces to the midchord of the gust vanes) of the lifting surfaces. The gust generator was driven by an Indiana General 48-V dc motor. A feedback control circuit was designed using classical techniques so that the gust generator frequency response was similar to that of a typical gust spectrum.

All compensator designs were implemented by a Wind River Systems VX Works UNIX-compatible real-time operating system running on a Heurikon HK68/V30 digital control computer. The Heurikon was linked to a Supercard array processor for increased controller speed. The control computer was capable of handling up to 16 sensor inputs (16-bit A/Ds) and eight control outputs (16-bit D/As). Variable frequency four-pole antialiasing Bessel filters were also utilized to eliminate unwanted alias signals. Three of the A/Ds were used to measure the input from the laser displacement sensors, and three of the D/As were used to output control signals to the power amplifiers that drove the three strain actuator groups (the sur-

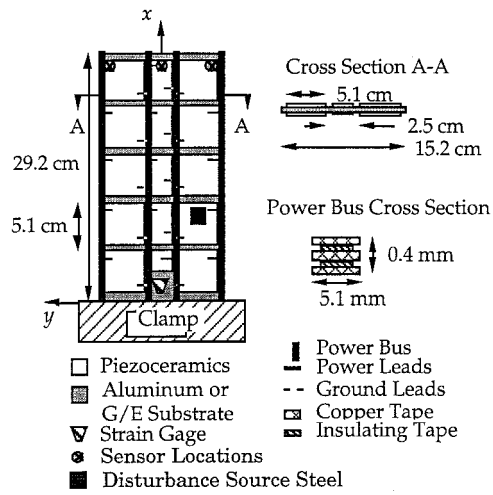

Fig. 1 Test article schematic.

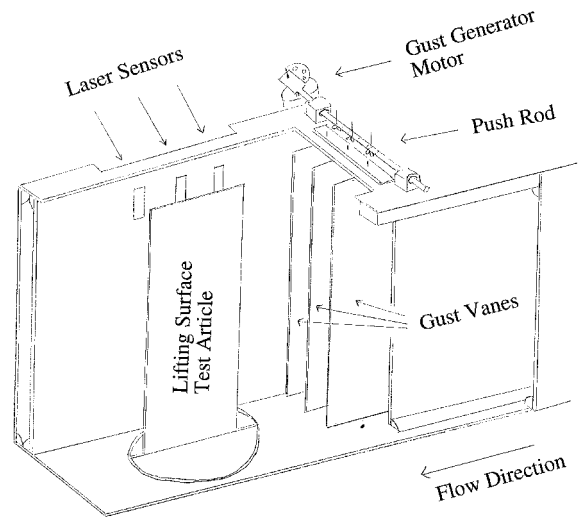

Fig. 2 Wind-tunnel test section with active lifting surface vertically mounted one semichord behind the gust generator vanes. The wall-mounted laser displacement sensors are also shown in the figure.

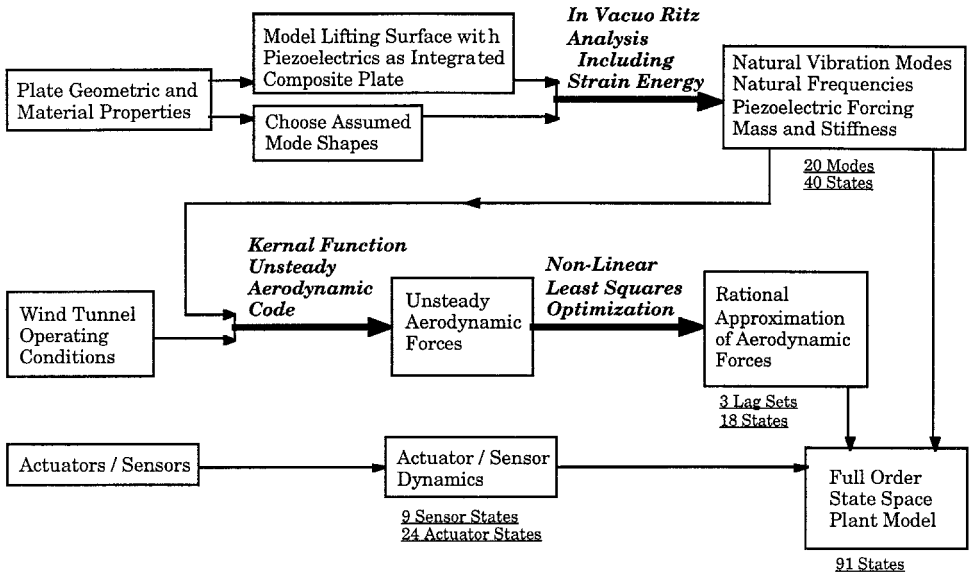

Fig. 3 Aeroelastic modeling flow chart. Figure shows structural, aerodynamic, and other component analytical models used to construct the full aeroelastic system.

face-bonded piezoelectrics were divided into leading edge u_1, midchord u_2, and training edge u_3 actuators groups). Thus, each controller designed was a three-input, three-output multivariable dynamic compensator.

A Tektronix 2630 Fourier analyzer was used to provide the input signal to the wind-tunnel gust generator. The Fourier analyzer was also used to process the disturbance, sensor, and control signals, and the output of the Fourier analyzer was used to produce disturbance and control transfer functions and to calculate the rms response.

Aeroelastic Model

The creation of an analytical aeroelastic model of sufficient accuracy for designing closed-loop controllers requires knowledge of structural dynamics, aerodynamics, and linear system analysis. Figure 3 shows the pieces of analysis needed and the logical flow of modeling tasks that lead to a high-fidelity aeroelastic model. Each piece contributes states, representing the dynamics of the physical phenomenon, to the model in a form compatible with linear time-invariant system analysis. The full system includes models of the plant (structural dynamics and unsteady aerodynamics), actuator and sensor dynamics, disturbance source dynamics, and any dynamics associated with electronic equipment such as amplifiers and filters. This section details the models used to describe the dynamics of the lifting surfaces, the assembly of the individual models into a coupled state-space system, and the reduction of the model to a size useful for designing effective control laws.

The Rayleigh–Ritz assumed mode model developed in Lazarus and Crawley[24] is used to describe the structural dynamics of the active lifting surface test articles. The Ritz model includes 20 assumed modes and makes use of experimental damping ζ_i and frequency ω_i values found from frequency response data. The governing equations are described with natural mode coordinates η in terms of the modal mass M, damping D, and stiffness K

$$M\ddot{\eta} + D\dot{\eta} + K\eta = F_\Lambda(t) + F_d(t) + F_A(t) \qquad (1)$$

where

$$M = \Phi^T m \Phi = \begin{bmatrix} \ddots & & \\ & m_r & \\ & & \ddots \end{bmatrix} = I$$

$$K = \Phi^T k \Phi = \begin{bmatrix} \ddots & & \\ & \omega_r^2 & \\ & & \ddots \end{bmatrix}$$

$$D = \begin{bmatrix} \ddots & & \\ & 2\zeta_r\omega_r & \\ & & \ddots \end{bmatrix} \qquad F = \Phi^T f$$

The structural system also can be expressed in the Laplace domain as

$$[Ms^2 + Ds + K]\eta(s) = F_\Lambda(s) + F_d(s) + F_A(s) \qquad (2)$$

where F_Λ, F_d, and F_A are the strain actuator, disturbance, and aerodynamic modal forcing matrices, respectively.

Calculating the unsteady forces acting on a lifting surface in a form compatible with modern linear time-invariant dynamic analysis and control law development routines requires a two-step process. First, the unsteady aerodynamic forces $F_A(k, M)$ resulting from wing motion and gust flow variation are found from three-dimensional compressible linear theory using either a doublet lattice[25] or kernel function[26] method. The unsteady forces, which are complex functions of reduced frequency $k = wb/U_\infty$ and Mach number $M = U_\infty/a_0$, are evaluated at several distinct reduced frequencies for each flight condition (wind speed and altitude). Second, the complex unsteady forcing matrices are fit with a rational function approximation in the (reduced) frequency domain. A variety of techniques have been developed to obtain accurate fits including linear and nonlinear least squares[27,28] and minimum state[29] methods.

The aerodynamic forces $F_A(k)$, which are comprised of forces generated by the lifting surface motion itself $F_{A\eta}(k)$ and unsteadiness in the flow $F_{Ag}(k)$, are included in the modal equations of motion [Eq. (1)] by premultiplying the aerodynamic forces by the transpose of the mass normalized in vacuo eigenvector matrix Φ:

$$\Phi^T F_A(k) = \Phi^T F_{A\eta}(k) + \Phi^T F_{Ag}(k) = qQ_\eta(k)\eta + qQ_g(k)_g \qquad (3)$$

In this study, the modal aerodynamic $Q_\eta(k)$ and gust force $Q_g(k)$ matrices were calculated using the kernel function unsteady aerodynamics code UNSAER.[30] The out-of-plane deflections of the natural elastic modes were evaluated and input to UNSAER along with the lifting surface geometry and the

reduced frequencies at which the aerodynamic forces are to be calculated. Aerodynamic forces were calculated for the first six natural elastic mode shapes and the sinusoidal gust. Only the first six natural modes were used in determining the aerodynamic forces because the deflections associated with higher modes did not generate any significant aerodynamic forces.

The unsteady kernel function code provides the complex modal aerodynamic forces acting on the lifting surface as a function of reduced frequency. These forces can be combined with the in vacuo modal mass, damping, and stiffness matrices to calculate the system stability, natural frequencies, and dynamic response. However, with the aerodynamic forces left as complex functions of reduced frequency, the dynamics of the system can only be determined using either the physical interpretation lacking $V-g$[31] or the time-consuming iterative $p-k$[32] method. Further, modern control law synthesis techniques cannot be utilized with the complex aerodynamic forcing matrices known only at discrete reduced frequencies. Therefore, it is essential that the unsteady aerodynamic forces, which are transcendental functions in the Laplace domain, are fit with rational approximations so that efficient linear time-invariant system algorithms (e.g., Matlab and MatrixX) may be utilized.

The unsteady forces are approximated with continuous functions by equating the complex forcing matrices with partial fraction frequency domain expansions, which are quadratic in reduced frequency k and have n_l lag terms

$$\begin{aligned} F_A(k) &= q[Q_\eta(k)]\eta + q[Q_g(k)]g \\ &= q\left[(A_0)_\eta + (A_1)_\eta k + (A_2)_\eta k^2 + \sum_{l=1}^{n_l}(A_{2+1})_\eta \frac{k}{k+R_l}\right]\eta \\ &\quad + q\left[(A_0)_g + (A_1)_g k + (A_2)_g k^2 + \sum_{l=1}^{n_l}(A_{2+1})_g \frac{k}{k+R_l}\right]g \end{aligned} \tag{4}$$

The coefficient matrices A_0, A_1, A_2, and A_{2+l} are solved for using a nonlinear least-squares technique, where the problem becomes nonlinear when the lag poles R_l are free parameters.

In this study, the nonlinear least-squares routine SPLFIT[27] was utilized to generate the rational approximation matrix coefficients and lag poles. The first coefficient matrix A_0 was fixed such that the approximation matched the steady-state solution exactly for k equal to zero. The remaining coefficient matrices were solved for by SPLFIT. It was found that the accuracy of the approximation improved as the number of lag terms n_l increased from zero. The accuracy of the fit, measured by the least-squares error between the rational approximation and the aerodynamic forces calculated at discrete reduced frequencies, improved with the addition of a first, second, and third lag term, but no measurable improvement was found with the addition of a fourth term. Hence, three lag terms were used in fitting the lifting surface test article unsteady aerodynamics.

With the aerodynamic forces computed and approximated by rational functions, the next step required to describe the (reduced) frequency-dependent unsteady aerodynamic forces in a form compatible with linear time-invariant system analysis methods is to express the approximate forcing functions [Eq. (4)] in terms of the Laplace variable s. The transformation to the Laplace domain is accomplished by letting $s = iw$ ($k = wb/U$). The final step in obtaining a state-space description is to describe the aerodynamic lag terms as augmented states. Following Tiffany and Adams,[27] the aerodynamic states are defined to combine both elastic and gust modes, thereby minimizing the number of states added. For each lag term, one state is augmented to the system for each mode fitted with aerodynamics. Thus, the total number of augmented aerodynamic states is equal to the number of lags times the number of fitted modes.

The aeroelastic behavior of the lifting surfaces test articles is analyzed by combining the structural and aerodynamic models in a state-space representation. The final state-space aeroelastic system includes both structural η and aerodynamic X_a states. The aerodynamic matrices combine with the structural matrices in the form of apparent mass, aerodynamic damping, aerodynamic stiffness, and aerodynamic lag-state terms. Only the aerodynamic states, which model the time delays between the wing motion and the aerodynamic forces created by the motion, increase the number of states needed to describe the system. However, the dynamic response is influenced by all of the aerodynamic terms, and instabilities are caused by both the nonsymmetric nature of the aerodynamic mass, damping, and stiffness terms, as well as the lag states.

Lifting Surface Aeroelastic Response

The dynamic response of the lifting surfaces can be studied by observing the movement of the system poles with airspeed. Such aerodynamic root loci are plotted in Fig. 4 for the aluminum and G/E test articles, respectively. In the figure, the poles are plotted for airspeeds from 0 to 100 mph at increments of 20 mph. Figure 4 shows that the aluminum lifting surface is far from any instabilities at the gust alleviation and command following test velocity of 60 mph. In fact, the poles of the aluminum lifting surface are predicted to be stable until the flutter (130 mph) and divergence (165 mph) speeds, which are well above the operating range of the wind tunnel (100 mph). The poles of the G/E lifting surface are also stable over the entire operating range of the wind tunnel. However, flutter and divergence are predicted to occur at the lower wind speeds of 110 and 115 mph, respectively.

On the other hand, the modified-for-flutter lifting surface, predicted to flutter at 87.6 mph, has the desired quality of actually fluttering within the limits of wind tunnel. Experimentally, the airspeed was increased until the test article went unstable, and severe vibrations were encountered that were limited only by the tunnel walls. The flutter speed for this wing was measured at 88 mph. The flutter mode was predicted and observed to be caused by a coalescence of the first bending and first torsion modes. The classical coalescence nature of this instability is clearly illustrated in Fig. 5, which plots the experimental, and analytical natural frequencies of the first two modes vs airspeed for the modified-for-flutter aluminum lifting surface, as well as the analytical damping ratios of the first four modes. As the wind speed becomes larger, the bending

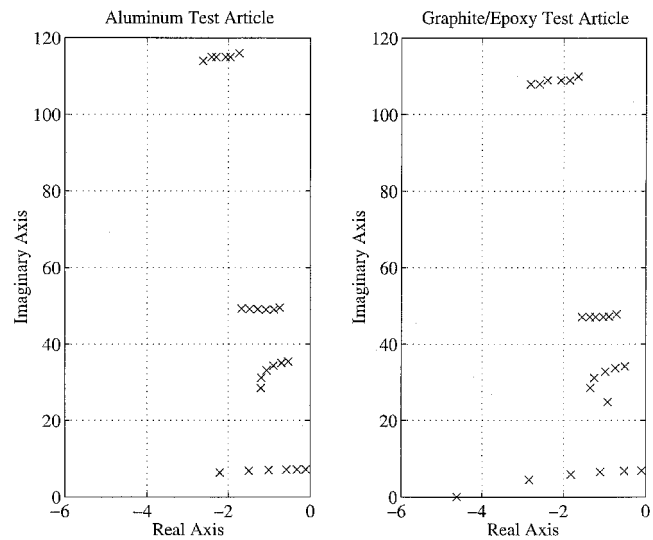

Fig. 4 Lifting surface pole movement for airspeeds increasing from zero to the wind-tunnel limit of 100 mph in increments of 20 mph. All poles are on the left of the imaginary axis, indicating that the system is stable.

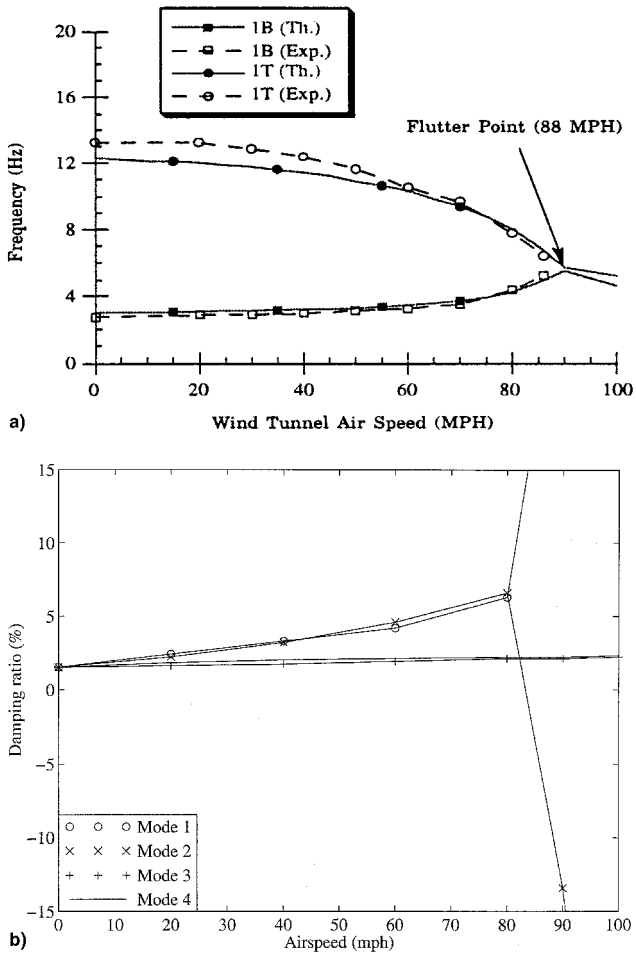

Fig. 5 a) Natural frequency of the modified-for-flutter aluminum lifting surface bending and torsion modes for airspeeds increasing from 0 to the wind-tunnel limit of 100 mph and b) damping ratio vs airspeed of the modified-for-flutter aluminum lifting surface.

frequency increases and the torsional frequency decreases until the two coalesce at the flutter speed when the damping ratio is negative.

Full-Order Analytic Model

The full-order wind-tunnel model had 93 states. Forty of the states were associated with the 20 structural modes, and 18 states were used to model the lags in the unsteady aerodynamics (A_p, B_p, L_p, and C_p). The remaining states resulted from the dynamics of the three laser sensors (one pole at 700 Hz) and antialiasing filters (two poles at 1000 Hz for each of the three sensors and two poles at 2500 Hz for each of the 12 possible control inputs). Note that only three of the 12 possible control inputs were utilized. Two additional states were included in the model to account for the roll-off of the gust spectrum produced by the gust generator. This full-order system evaluation model (A, B, L, and C) was used to calculate the disturbance transfer functions and to evaluate the stability and performance of the control laws designed. The dynamics of this large-order system can be described in either a state-space

$$\dot{x} = Ax + Bu + Ld \qquad y = Cx \tag{5}$$

or transfer function representation

$$\begin{aligned} y &= G_c(s)u \qquad G_c = C(sI - A)^{-1}B \\ y &= G_d(s)d \qquad G_d = C(sI - A)^{-1}L \end{aligned} \tag{6}$$

where $G_c(s)$ contains the control and $G_d(s)$ holds the disturbance transfer functions.

Model Order Reduction

The use of large-order evaluation models for developing model-based control laws usually leads to similarly large-order compensators, which are difficult to implement and unnecessary for obtaining effective controllers. Thus, the 93 state evaluation models were reduced to lower-order design models. The reduction was based on the Hankel singular values of the systems. This procedure reduced the 93 state evaluation models to 32, 34, and 38 states design models for the aluminum, G/E, and modified-for-flutter wind-tunnel evaluation models, respectively. It was found that the disturbance to sensor output (y/d) and control input to sensor output (y/u) transfer functions of the design models were effectively identical to those of the evaluation models in the evaluation bandwidth (200 Hz).

Wind-Tunnel Experiments

Three sets of wind-tunnel investigations were performed. First, gust alleviation experiments were carried out to show the ability of strain actuation to attenuate simulated atmospheric gusts. Second, command following experiments were performed to access the ability of active lifting surfaces to follow commands typical of those required for aircraft maneuverability. Third, flutter suppression experiments were conducted to not only demonstrate flutter suppression, but also to show that the response of initially unstable plants to disturbances in the airstream could be suppressed using strain actuation. The wind-tunnel experiments served to both validate the analytical aeroelastic models and demonstrate the ability of distributed strain actuators to control aeroelastic lifting surfaces. Since effective model-based compensators can only be derived from accurate models, the ability to implement effective controllers simultaneously demonstrates modeling and control capabilities. The gust alleviation and flutter suppression experiments are presented in this paper, whereas the command following experiments, which have been omitted because of space constraints, can be found in Lazarus.[33]

Compensator Design

The unsteady aerodynamic forces created by the lifting surface motion were found to add large amounts of damping to the first bending and torsion modes at the gust alleviation test velocity of 60 mph. The fact that these low-frequency modes are so heavily damped, along with the large low-frequency disturbance forces created by the gust generator, means that large actuator forces must be applied by the strain actuators to achieve significant disturbance attenuation. These large actuator forces can be created by designing compensators with large low-frequency gain. However, the compensator gain must roll-off without destabilizing the high-frequency modes, which are not heavily influenced by the aerodynamics and remain lightly damped. The combination of requiring large low-frequency compensator gains and needing to roll-off the compensator through lightly damped modes makes the problem of achieving good gust alleviation performance while maintaining stability robustness very challenging.

MIMO compensators for the gust alleviation and flutter suppression experiments were designed using LQG optimal control theory. Each compensator utilized inputs from the three laser sensors and generated three outputs for the power amplifiers driving the strain actuator control groups (see the Test Configuration section). Each three-input, three-output compensator was reduced from the design model order to a 14-state compensator for implementation on the Heurikon control computer. The compensators designed were evaluated analytically using the 93-state, full-order aeroelastic evaluation model and experimentally in the wind tunnel over the 200-Hz evaluation bandwidth. Further compensator design details can be found in Lazarus.[33]

The state cost was chosen as the sum of the output y rms response squared for the gust alleviation and flutter suppression experiments. Similarly, the control cost was chosen to be the sum of the control u rms response squared. The total cost J was therefore

$$J = \int_0^\infty (\bar{y}^T\bar{y} + \rho\bar{u}^T\bar{u})\,\mathrm{d}t = \int_0^\infty (x^TQx + ru^TRu)\,\mathrm{d}t$$
$$Q = (C/y_{\max})^T(C/y_{\max}) \qquad R = I/u^2_{\max} \tag{7}$$

where ρ is the relative state to control weighting design parameter. The scaled outputs $\bar{y}$ and inputs $\bar{u}$ were calculated by normalizing the physical outputs and inputs by their maximum values. The cost defined in Eq. (7) was used to design the LQR full-state feedback portion of the LQG compensators, where the control weight ρ was a free design parameter. A Kalman filter was designed to estimate the states for each compensator using the measurement noise as the free design variable.

Gust Alleviation Performance Results

This section describes the control laws designed and tested to demonstrate subcritical gust alleviation. The performance measure is an rms value of the tip displacement at the leading edge, trailing edge, or the midchord as measured by the laser sensors. Figures 6 and 7 display the analytical and experimental open- and closed-loop response for the gust alleviation experiments from the gust generator input d to the leading-edge laser sensor y_1. The design airspeed for the control laws was 60 mph, which was the maximum speed at which the gust generator functioned effectively. The open-loop response was calculated analytically from Eq. (6) and the closed-loop response was calculated analytically from a state-space representation of the closed-loop system

$$\begin{bmatrix}\dot{x}\\ \dot{\hat{x}}\end{bmatrix} = \begin{bmatrix}A - BD_cC & -BF_c\\ K_cC & A_{cc}\end{bmatrix}\begin{bmatrix}x\\ \hat{x}\end{bmatrix} + \begin{bmatrix}L\\ 0\end{bmatrix} d$$
$$y = [C \quad 0]\begin{bmatrix}x\\ \hat{x}\end{bmatrix} \tag{8}$$

where the compensator dynamics are represented by

$$\dot{\hat{x}} = A_{cc}\hat{x} + K_ce \qquad u = F_c\hat{x} + D_ce \tag{9}$$

The error signal e is equal to the command, for gust alleviation this is zero, minus the sum of the output y and the measurement noise θ. The experimental response was measured in the wind tunnel using the Tektronix Fourier analyzer. The compensators used to produce the transfer functions shown in these figures were designed using a control weight ρ of 10^{-1} and a sensor noise of 1.0%. The gust response transfer functions show both the accuracy of the aeroelastic analytical model and the ability of the actively controlled lifting surfaces to alleviate gust disturbances.

The active lifting surface gust alleviation effectiveness can be observed from the first bending and quasisteady response in Figs. 6 and 7. For both lifting surfaces, controllers are shown that reduce the response of the first bending mode by

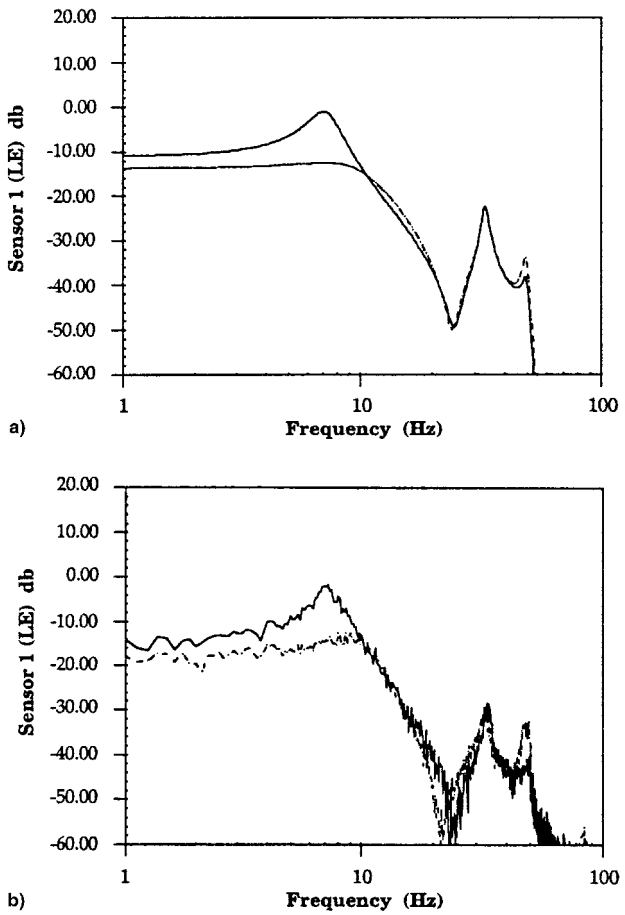

Fig. 6 Open- and closed-loop frequency response of the aluminum lifting surface for a LQG gust alleviation compensator designed with $\rho = 10^{-1}$ and a sensor noise of 1.0%: a) analytic and b) experimental frequency responses.

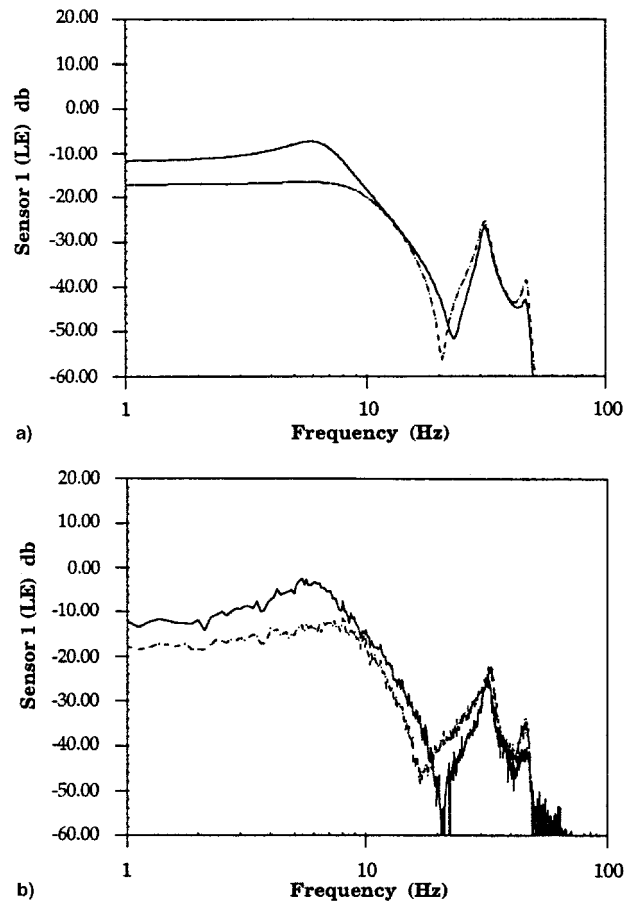

Fig. 7 Open- and closed-loop frequency response of the G/E lifting surface for a LQG gust alleviation compensator designed with $\rho = 10^{-1}$ and a sensor noise of 1.0 percent: a) analytic and b) experimental frequency responses.

approximately 10 db, even though there was already considerable open-loop damping in this mode of the aluminum (14%) and G/E (29%) test articles. Control effectiveness is also shown in the quasisteady response, which improved the open-loop response by 3 db for the aluminum and 6 db for the G/E test article. Note that the G/E lifting surface was more effective in controlling the quasisteady response because of its bending/twist coupling.

It was also expected that the G/E plate bending/twist coupling would allow for enhanced control of the torsional vibration modes. However, this control was not realized because the gust forces barely excited the torsional modes (compared to the first bending mode), which caused the compensators designed to only attempt to effect control of the bending mode. In fact, so much of the vibration energy, and therefore, the cost, was associated with the first bending mode and quasisteady response that other modes were purposely destabilized (but not made unstable) in favor of applying more control to the first bending mode and quasisteady response.

The performance shown by the 60-mph gust disturbance response transfer functions can be quantified and correlated with the control authority needed and the maximum control authority available by plotting the state cost vs control cost. Wind-tunnel gust alleviation cost curves identify the incremental state cost reduction obtained from increased control authority. Analytical and experimental cost curves for the gust alleviation compensators are shown in Fig. 8 for the aluminum and G/E lifting surfaces. The analytic cost curves were calculated by solving the Lyapunov problem associated with the following closed-loop system:

$$\begin{bmatrix} \dot{x} \\ \dot{\hat{x}} \end{bmatrix} = \begin{bmatrix} A - BD_cC & -BF_c \\ K_cC & A_{cc} \end{bmatrix} \begin{bmatrix} x \\ \hat{x} \end{bmatrix} + \begin{bmatrix} L & -BD_c \\ 0 & K_c \end{bmatrix} \begin{bmatrix} d \\ \theta \end{bmatrix} \tag{10}$$

where the state and control costs can be found directly from the covariance matrices[34]:

$$\begin{aligned} \text{state cost} &= \text{trace}(QE[xx^T]) \\ \text{control cost} &= (1/\rho)\text{trace}(GR^{-1}G^TE[\hat{x}\hat{x}^T]) \end{aligned} \tag{11}$$

The experimental values were found from the rms sensor outputs and control inputs measured over the evaluation bandwidth (200 Hz). Figures 6 and 7 show that the analytical and experimental results agree well and that significant disturbance attenuation was achieved despite the high open-loop damping in the lower modes. Note that all values were normalized by the open-loop state cost, so that the control cost is unity when using a control gain of zero.

Experimental results are plotted in Fig. 8 for controllers designed with control weights of 1.0 and 10^{-1} for the aluminum and 10^{1}, 1.0, and 10^{-1} for the G/E lifting surface. The highest performing gust alleviation compensator designs ($\rho = 10^{-1}$) were analytically predicted to reduce the aluminum lifting surface state cost by 77.3% (52.3% rms) or 6.4 db, and the G/E lifting surface compensator was predicted to reduce the state cost by 84.1% (60.1% rms) or 8.0 db. The aluminum lifting surface multivariable compensator was experimentally found to reduce the state cost by 79.2% (54.3% rms) or 6.8 db, whereas the G/E lifting surface multivariable compensator was able to reduce the state cost by 83.6% (59.6% rms) or 7.9 db.

Flutter Suppression Performance Results

After completing the wind-tunnel gust alleviation experiments, a lead mass was attached to the aluminum lifting surface for the purpose of performing flutter experiments (see the Test Configuration section). The added mass lowered the flutter speed of this modified-for-flutter lifting surface to 88 mph. The gust generator was removed from the wind tunnel for the flutter suppression experiments since the gust vanes themselves fluttered at about 80 mph. Therefore, the disturbance source for the flutter experiments was generated only by the turbulence in the freestream flow, which produced significant disturbance forces because of the high speeds (relative to the tunnel maximum speed of 100 mph) at which the flutter suppression experiments were conducted.

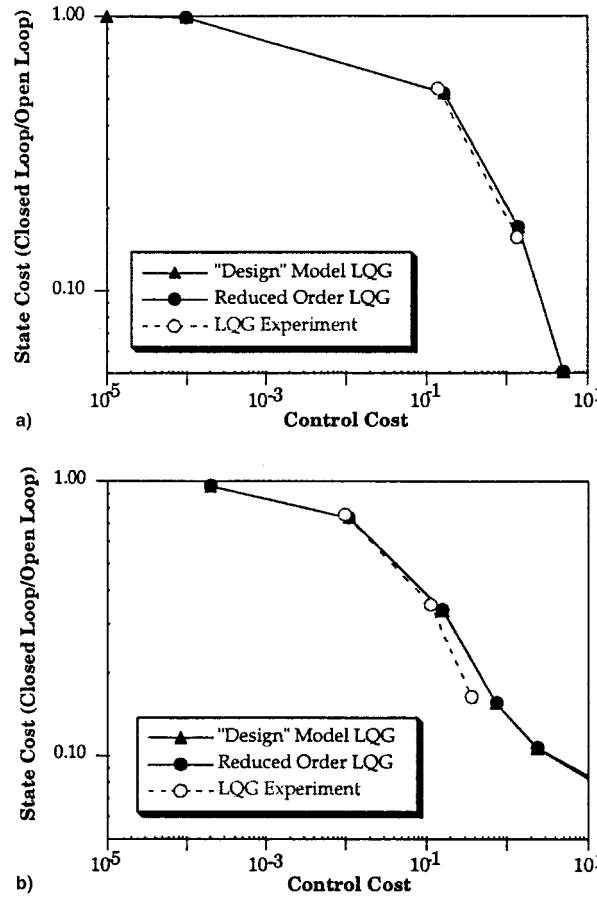

Fig. 8 Analytical and experimental state vs control closed-loop cost curves for active lifting surface gust alleviation compensators designed with a sensor noise of 1.0%: a) aluminum and b) G/E lifting surfaces.

As an initial design point, a design airspeed immediately postflutter was chosen as 90 mph with the intention of testing this control law at 90 mph and at speeds beyond 90 mph until actual instability occurred. Three-input, three-output multivariable flutter suppression controllers were designed. The flutter suppression controllers were evaluated analytically for stability and performance at 80 and 85 mph, as well as at the design point. All compensators were predicted analytically and found experimentally to be stable at both 80 and 85 mph. Therefore, the experimental procedure was as follows: first, the airspeed was set at 80 mph and the open-loop response of the lifting surface, caused by the flow turbulence, was measured. Then, the control computer was turned on and the wind speed was slowly raised to the flutter suppression design speed of 90 mph. At the design speed, the rms sensor outputs and control inputs were measured. Finally, the wind speed was increased until either the system became unstable or the tunnel limit was reached.

The results of the wind-tunnel flutter suppression experiments are reported by plotting closed-loop state vs control cost curves, similar to those reported for the wind-tunnel gust alleviation tests. The costs curves show the incremental improvement of the state cost (reduction in rms response) as the control effort is increased. As before, the analytical costs were

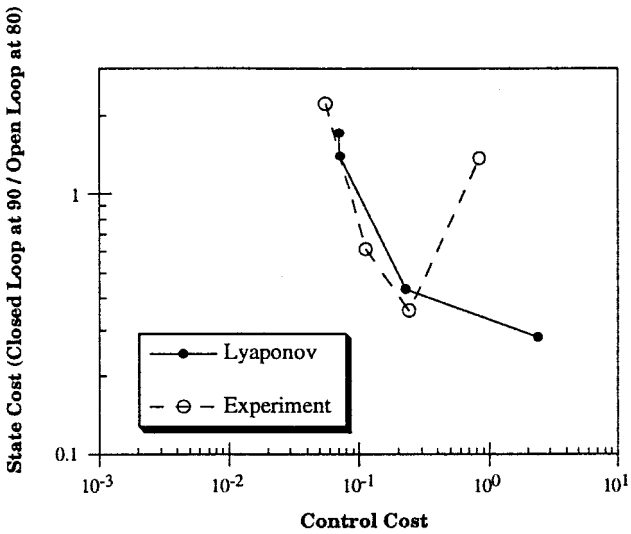

Fig. 9 Analytical and experimental state vs control closed-loop cost curves for the modified-for-flutter aluminum lifting surface 90-mph flutter suppression experiments.

calculated by inserting the compensators and the full-order aeroelastic models into Eqs. (10) and (11), and the experimental costs were found by measuring the rms sensor outputs and control inputs (200-Hz evaluation bandwidth). Unlike the previous tests, however, there is no open-loop state cost by which the results can be normalized since the open-loop system is unstable at 90 mph. Thus, the closed-loop costs are normalized by the open-loop state cost at 80 mph. In addition, the open-loop state cost is not recovered and the control gains do not go to zero as ρ becomes large, because the open-loop system is unstable. Instead, some amount of control authority is needed, indicated by a finite control cost and a vertical asymptote of the cost curve, to stabilize the system.

Figure 9 displays the analytical and experimental cost curves for the modified-for-flutter aluminum lifting surface tested at 90 mph with compensators designed using a sensor noise of 1.0%. Observe that stable flutter suppression compensators (finite state costs) have been designed and implemented, and that agreement between the analysis and experiment is quite good. Also note that the figure shows the minimum control effort needed to stabilize the initially unstable system, indicated by the low control weight asymptote. Compensators designed with control weights greater than 1.0 are observed only to have enough control authority to stabilize the system. However, as the control weight is decreased, higher gain compensators are designed that are capable of not only stabilizing the system, but also of reducing the disturbance response. The disturbance response continues to decrease as the control weight is decreased (gains increase) until the minimum response design is found ($\rho = 10^{-2}$). Note that compensators with higher gains ($\rho = 10^{-4}$) were analytically predicted to further decrease the state cost, however, stability robustness issues prevented any of these designs from actually achieving better performance. The figure shows that these designs either destabilize high-frequency modes (the design with an experimentally measured high state cost and high control cost) or were unstable (not shown).

The compensator design ($\rho = 10^{-2}$), which stabilized the system at 90 mph and minimized the disturbance response, was analytically predicted to decrease the state cost from that of the 80-mph open-loop system by 71.9% (47.0% rms) or 5.5 db. This compensator was found experimentally to stabilize the system and reduce the disturbance response by 76.0% (51.0% rms) or 6.2 db. In addition, this controller was able to suppress flutter up to 98 mph, 11% above the flutter speed and 9% above the 90-mph airspeed for which the compensator was designed.

Conclusions

The work presented shows the validity of the aeroelastic modeling procedure presented and demonstrates the ability of strain-actuated active lifting surfaces to effect a variety of aeroelastic control objectives such as gust alleviation and flutter suppression. The active lifting surfaces were able to attenuate the rms gust response by over 60%, and were able to suppress flutter while significantly reducing the disturbance response. The flutter speed was increased by 11%.

These results may only be generalized to other lifting surfaces with the same nondimensional parameters, such as aspect ratio, thickness ratio, force stiffness ratio, and force pressure ratio. In certain applications, such as panel flutter or stabilizer control, scaling the results may require little effort because the geometric parameters are similar. However, scaling the results for some applications may be problematic. For example, typical wings are made of box-beam construction and have thickness ratios of at least 2%. To apply the results of the test articles (thickness ratio of 0.5%) to such a wing, the actuator thickness would have to be considerably larger to match the force stiffness ratio. On the other hand, engineering ingenuity can be applied to increase control authority using other mechanisms, such as increasing the bending/twist coupling or actuation strain.

Final concerns are those of realizable aeroelastic sensors, actuator power, and added actuator weight. For this study, laser displacement sensors were used that are not realizable for true aeroelastic control situations. Future investigations should implement similar control laws with aeroelastic sensors such as strain gauges and accelerometers. Furthermore, the power requirements of these control laws and the piezoceramics have not been studied. A comparison of the power needs and performance of strain actuation vs conventional aerodynamic surface actuation needs to be made. Finally, with a density more than twice that of aluminum, piezoceramics are hardly the ideal aerospace material. The implications of such a large actuator weight penalty have been largely ignored in this study, but should be investigated thoroughly. One can only hope that recent advances in material science are able to provide improved strain actuators that are lightweight, high strength, and have high actuation strains, because this is what is needed to make strain-actuated aeroelastic control a truly useful technology.

References

[1]Noll, T. E., "Aeroservoelasticity," *Proceedings of the AIAA 31st Structures, Structural Dynamics, and Materials Conference* (Long Beach, CA), AIAA, Washington, DC, 1990, pp. 1560–1570.

[2]Horikawa, H., and Dowell, E. H., "An Elementary Explanation of the Flutter Mechanism with Active Feedback Controls," *Journal of Aircraft*, Vol. 16, No. 4, 1979, pp. 225–232.

[3]Ohta, H., Fujimori, A., Nikiforuk, P. N., and Gupta, M. M., "Active Flutter Suppression for Two-Dimensional Airfoils," *Journal of Guidance, Control, and Dynamics*, Vol. 12, No. 2, 1989, pp. 188–194.

[4]Heeg, J., "An Analytical and Experimental Study to Investigate Flutter Suppression Via Piezoelectric Actuation," M.S. Thesis, George Washington Univ., Washington, DC, 1991.

[5]Newsom, J. R., Pototzky, A. S., and Abel, I., "Design of a Flutter Suppression System for an Experimental Drone Aircraft," *Journal of Aircraft*, Vol. 22, No. 5, 1985, pp. 380–386.

[6]Mahesh, J. K., Stone, C. R., Garrard, W. L., and Dunn, H. J., "Control Law Synthesis for Flutter Suppression Using Linear Quadratic Gaussian Theory," *Journal of Guidance and Control*, Vol. 4, No. 4, 1981, pp. 415–422.

[7]Trame, L. W., Williams, L. E., and Yurkovich, R. N., "Active Aeroelastic Oscillation Control on the F/A-18 Aircraft," *Proceedings of the AIAA Guidance, Navigation, and Control Conference* (Snowmass, CO), AIAA, New York, 1985, pp. 94–104.

[8]Liebst, B. S., Garrard, W. L., and Adams, W. M., "Design of an Active Flutter Suppression System," *Journal of Guidance, Control, and Dynamics*, Vol. 9, No. 1, 1986, pp. 64–71.

[9]Ghiringhelli, G. L., Lanz, M., and Mantegazza, P., "Active Flutter Suppression for a Wing Model," *Journal of Aircraft*, Vol. 27, No. 4, 1990, pp. 334–341.

[10]Peloubet, R. P., Haller, R. L., and Bolding, R. M., "On-Line Adaptive Control of Unstable Aircraft Wing Flutter," *Proceedings of the IEEE Conference on Decision and Control*, Vol. 2, 1990.

[11]Ueda, T., Matsushita, H., Suzuki, S., and Miyazawa, Y., "ACT Wind-Tunnel Experiments of a Transport-type Wing," *Journal of Aircraft*, Vol. 28, No. 2, 1991, pp. 139–145.

[12]Suzuki, S., and Matsuda, S., "Structure/Control Design Synthesis of Active Flutter Suppression by Goal Programming," *Journal of Guidance, Control, and Dynamics*, Vol. 14, No. 6, 1991, pp. 1260–1266.

[13]Karpel, M., "Design for Active Flutter Suppression and Gust Alleviation Using State-Space Aeroelastic Modeling," *Journal of Aircraft*, Vol. 19, No. 3, 1982, pp. 221–227.

[14]Matsuzaki, Y., Ueda, T., Miyazawa, Y., and Matsushita, H., "Gust Load Alleviation of a Transport-Type Wing: Test and Analysis," *Journal of Aircraft*, Vol. 26, No. 4, 1989, pp. 322–327.

[15]Waszak, M. R., and Srinathkumar, S., "Flutter Suppression for the Active Flexible Wing: Control System Design and Experimental Validation," *Proceedings of the AIAA Dynamics Specialists Conference* (Dallas, TX), AIAA, Washington, DC, 1992, pp. 138–145.

[16]Christhilf, D. M., and Adams, W. M., Jr., "Multifunction Tests of a Frequency Domain Based Flutter Suppression System," *Proceedings of the AIAA Dynamics Specialist Conference* (Dallas, TX), AIAA, Washington, DC, 1992, pp. 146–155.

[17]Mukhopadhyay, V., "Flutter Suppression Digital Control Law Design and Testing for the AFW Wind-Tunnel Model," *Proceedings of the AIAA Dynamics Specialists Conference* (Dallas, TX), AIAA, Washington, DC, 1992, pp. 156–161.

[18]Lazarus, K. B., Crawley, E. F., and Bohlmann, J. D., "Static Aeroelastic Control Using Strain Actuated Adaptive Structures," *Journal of Intelligent Material Systems and Structures*, Vol. 2, No. 3, 1991, pp. 386–410.

[19]Ehlers, S. M., and Weisshaar, T. A., "Effect of Adaptive Material Properties on Static Aeroelastic Control," *Proceedings of the AIAA 33rd Structures, Structural Dynamics, and Materials Conference* (Dallas, TX), AIAA, Washington, DC, 1992, pp. 914–924.

[20]Kwakernaak, H., and Sivan, R., *Linear Optimal Control Systems*, Wiley-Interscience, New York, 1972.

[21]Doyle, J. C., Glover, K., Khargonekar, P. P., and Francis, B. A., "State-Space Solutions to Standard H_2 and H_∞ Control Problems," *IEEE Transactions on Automatic Control*, Vol. AC-34, No. 8, 1989, pp. 831–847.

[22]Hyland, D. C., and Bernstein, D. S., "The Optimal Projection Equations for Fixed-Order Dynamic Compensation," *IEEE Transactions on Automatic Control*, Vol. AC-29, No. 11, 1985, pp. 1034–1037.

[23]Lazarus, K. B., and Crawley, E. F., "Induced Strain Actuation of Composite Plates," Massachusetts Inst. of Technology, Gas Turbine Lab., Rept. 197, Cambridge, MA, 1989.

[24]Lazarus, K. B., and Crawley, E. F., "Multivariable High-Authority Control of Plate-Like Active Structures," *Proceedings of the AIAA 33rd Structures, Structural Dynamics, and Materials Conference* (Dallas, TX), 1992, pp. 931–945.

[25]Albano, E., and Rodden, W. P., "A Doublet-Lattice Method for Calculating Lift Distributions on Oscillating Surfaces in Subsonic Flows," *AIAA Journal*, Vol. 7, No. 2, 1969, pp. 279–285; also "Double-Lattice Method for Calculating Lift Distributions or Oscillating Surfaces for Subsonic Flows," Errata, *AIAA Journal*, Vol. 7, No. 11, 1969, p. 2192.

[26]Watkins, C. E., Woolston, D. S., and Cunningham, J. J., "A Systematic Kernel Function Procedure for Determining Aerodynamic Forces on Oscillating or Steady Finite Wings at Subsonic Speeds," NASA TR-48, 1959.

[27]Tiffany, S. H., and Adams, W. M., Jr., "Nonlinear Programming Extensions to Rational Function Approximation Methods for Unsteady Aerodynamic Forces," NASA TP-2776, July 1988.

[28]Eversman, W., and Tewari, A., "Consistent Rational-Function Approximation for Unsteady Aerodynamics," *Journal of Aircraft*, Vol. 28, No. 9, 1991, pp. 545–552.

[29]Karpel, M., and Hoadley, S. T., "Physically Weighted Approximations of Unsteady Aerodynamic Forces Using the Minimum-State Method," NASA TP-3025, March 1991.

[30]Cunningham, A. E., "A Collocation Method for Predicting Subsonic Pressure Distribution on Interfering Parallel Wings," *Proceedings of the AIAA 12th Structures, Structural Dynamics, and Materials Conference*, AIAA, New York, 1971.

[31]Bisplinghoff, R. L., Ashley, H., and Halfman, R. L., *Aeroelasticity*, Addison–Wesley, Reading, MA, 1957.

[32]Hassig, H. J., "An Approximate True Damping Solution of the Flutter Equation by Iteration," *Journal of Aircraft*, Vol. 8 No. 11, 1971, pp. 885–889.

[33]Lazarus, K. B., "Multivariable High-Authority Control of Plate-Like Active Lifting Surfaces," Ph.D. Dissertation, Massachusetts Inst. of Technology, Cambridge, MA, June 1992.

[34]Kwakernaak, H., and Sivan, R., *Linear Optimal Control Systems*, Wiley-Interscience, New York, 1972.